JOURNAL OF THERMOPHYSICS AND HEAT TRANSFER
Vol. 22, No. 3, July–September 2008

Microchannel Heat Sink with Designed Roughness: Analysis and Optimization

Afzal Husain* and Kwang-Yong Kim†
Inha University, Incheon 402-751, Republic of Korea

DOI: 10.2514/1.34678

A microchannel heat sink with rib structures is investigated numerically for thermal resistance and pumping power. Multi-objective shape optimization of a staggered-rib microchannel heat sink is performed using a multi-objective evolutionary algorithm. Three design variables (i.e., ratios of the rib height to width of channel, width to height of the rib, and channel width to pitch of the rib) are selected for optimization. Thermal resistance and pumping power are taken as objective functions. Navier–Stokes and energy equations for laminar flow and conjugate heat transfer are solved for flow analyses using a finite volume solver. Thermal resistance is decreased and the Nusselt number is increased at the expense of pressure drop in a ribbed microchannel. Thermal resistance in a ribbed channel is generally higher than that in a smooth channel for fixed pumping power, but the difference in thermal resistance reduces as pumping power increases. The design variable of the ratio of rib height to width of channel is primarily responsible for and the most sensitive to the heat transfer augmentation, whereas ratios of width to height of the rib and channel width to pitch of the rib are found to be less sensitive in the design space. The ratio of channel width to pitch of the rib is found to be the most Pareto-sensitive (sensitive along the Pareto-optimal front), whereas the ratio of width to height of the rib is found to be the least Pareto-sensitive.

Nomenclature

A_c	=	cross-sectional area of the microchannel
A_s	=	surface area of the substrate base
C_p	=	specific heat
d_h	=	hydraulic diameter
E	=	error vector
G	=	$(\theta^2 + 1)/(\theta + 1)^2$
h_{rib}	=	height of the rib
h_{conv}	=	convective heat transfer coefficient
H_c	=	microchannel depth
$\mathbf{I}$	=	identity matrix
k	=	thermal conductivity
L_x	=	length of the heat sink
L_y	=	width of the heat sink
L_z	=	height of the heat sink
M	=	number of objective functions
N	=	number of dimensions in design space
Nu	=	Nusselt number
n	=	number of microchannels
P	=	pumping power
p	=	pressure
p_{rib}	=	pitch of the ribs
Pr	=	Prandtl number
q	=	heat flux
R^2	=	coefficient of multiple determination
R^2_{adj}	=	adjusted value of R^2
Re	=	Reynolds number
R_{th}	=	thermal resistance
T	=	temperature
u	=	liquid velocity in the microchannel
V	=	variance
$\bar{V}$	=	velocity vector
w_{rib}	=	width of the rib
W_c	=	width of the microchannel
W_w	=	fin width
x, y, z	=	orthogonal coordinate system
α	=	ratio of the rib height to width of channel
β	=	ratio of the rib width to height
ε	=	error
ϕ	=	ratio of fin width to depth of channel
γ	=	ratio of channel width to pitch of the rib
μ	=	dynamic viscosity
θ	=	ratio of channel width to depth
ρ	=	density
σ	=	standard deviation
ζ	=	estimated parameters

Subscripts

avg	=	average value
b	=	bulk value
f	=	fluid
fd	=	fully developed
i	=	inlet
max	=	maximum value
mean	=	mean value
o	=	outlet
s	=	substrate
sc	=	smooth microchannel
sf	=	solid–liquid interface
$w1$	=	microchannel side-wall 1
$w2$	=	microchannel side-wall 2

Received 19 September 2007; revision received 30 March 2008; accepted for publication 30 March 2008.

*Graduate Student, Department of Mechanical Engineering, 253 Yonghyun-Dong, Nam-Gu.

†Professor, Department of Mechanical Engineering, 2253 Yonghyun-Dong, Nam-Gu; kykim@inha.ac.kr. Member AIAA (Corresponding Author).

I. Introduction

RECENT developments in microelectromechanical systems (MEMS) and advanced ultra-large-scale integration technologies and devices associated with microminiaturization have led to significant improvement in packing densities. However, stacking of high-performance microprocessors seems to be limited by thermal density, because the operation of most electronic devices is strongly influenced by their temperature and surrounding thermal environment. Moreover, the eagerness for higher flux dissipation from a

microcooling device used in various systems such as micro-refrigerators, avionics, robotics, medicine, and the electronic industry and limitations of space in these devices led to the new designs for minichannels and microchannel heat sinks. Sophisticated fabrication processes have yielded economically competitive microchannels with a high surface-area-to-volume ratio and opened the way to implement new designs in silicon-based microcooling systems.

The potential of the microchannel heat sinks as heat transfer devices has motivated many researchers to analyze microcooling phenomena and to conduct parametric studies. Tuckerman and Pease [1] first realized the potential of this technology and laid a foundation for silicon-based microchannel heat sink experimentation. They experimented on a 56-μm-wide, 320-μm-deep microchannel fabricated by a chemical-etching process. Samalam [2] reported correlations for thermal resistance based on a theoretical study of the microchannel. Weisberg et al. [3] presented a design algorithm for the selection of a rectangular microchannel heat exchanger using a two-dimensional conjugate heat transfer model. Some analytical studies [4–6] have focused on modeling of the heat transfer and optimization of the microchannel geometry. Kawano et al. [7] performed both experimental and numerical studies for pressure drop and thermal resistance for a microchannel heat sink. Qu and Mudawar [8] computed three-dimensional fluid flow and heat transfer for a microchannel with a rectangular cross section. The ever-growing demand for higher heat flux dissipation has compelled the researchers to investigate alternative heat transfer enhancement techniques for these applications.

Recently, the microchannels have been investigated for passive surface microstructures such as dimples, pin fins, and ribs for surface heat transfer augmentation. Wei et al. [9] investigated heat transfer augmentation inside a microchannel with a dimpled surface for steady laminar flow in a rectangular microchannel. They found secondary and recirculatory flow structures and discussed a heat transfer enhancement mechanism. Cheng [10] simulated a two-layer stacked microchannel heat sink with enhanced-mixing passive microstructures. These structures led to higher heat transfer and lower thermal resistance. Wang et al. [11] investigated friction characteristics in a microchannel with various roughness elements for two-dimensional single-phase flow. Liou et al. [12] investigated Nusselt number distribution for vortex generators arranged on one wall of a square channel at a Reynolds number of 1.2×10^4. They computed 12 configurations of a single longitudinal vortex generator for heat transfer augmentation in a square channel. They found that the direction and strength of secondary flow were dominant among the various effective factors to heat transfer enhancement in a square channel. Ligrani et al. [13] carried out an exhaustive review of heat transfer augmentation techniques and observed that recirculation and shear layer reattachment are significant phenomena in heat transfer enhancement around the rib. These investigations have motivated the application of microribs in the microchannel heat sink for heat transfer augmentation.

Optimization methods with numerical analyses [14] are regarded as general design tools and offer a number of advantages, including automated design capability, varieties of constraints, and multi-objective applications. Liu and Garimella [15] presented analytical models and compared these models with the more robust three-dimensional numerical model and optimized the microchannel geometry. Kim [16] presented optimization procedure for a rectangular microchannel heat sink based on fin model, porous medium model, and numerical analysis at constant pumping power. He found that the assumptions used in the fin model are invalid for a large-aspect-ratio microchannel, and he used a polynomial function to approximate objective function in the given direction for the numerical model. In an attempt to optimize the shape of the microchannel, Li and Peterson [17] carried out a parametric study on the geometry of the rectangular microchannel at constant pumping power to find the optimal thermal resistance. Husain and Kim [18] presented single-objective optimization of the microchannel heat sink based on the surrogate methods. These studies reveal that pressure- and/or pumping-power-constrained optimization limit the applicability of the pumping source used at the microlevel. On the other hand, multi-objective optimization eliminates these constraints and provides a group of optimal solutions at various values of objective functions and constraints. These advantages associated with the multi-objective optimization provide impetus to the application of a multi-objective evolutionary algorithm (MOEA) to investigate a ribbed microchannel heat sink. The evolutionary algorithm has been used as an effective tool for generating global Pareto-optimal solutions in various engineering designs. Foli et al. [19] performed shape optimization of a microheat exchanger and obtained Pareto-optimal solutions using a fast and elitist nondominated sorting genetic algorithm (NSGA-II) [20] in combination with analytical and computational fluid dynamics (CFD) analysis.

The present work deals with the application of a microrib in the microchannel heat sink. Heat transfer enhancement analysis and multi-objective optimization of the ribbed microchannel were performed. The optimization methods involve the usage of hybrid MOEA [21] in combination with three-dimensional Navier–Stokes analysis and a surrogate model. As a surrogate model, response-surface approximation (RSA) [22] is used to evaluate objective function values required by the evolutionary algorithm to search optimal solutions. A hybrid multi-objective evolutionary approach is implemented using NSGA-II and a local search strategy. The global Pareto-optimal front is explored to get inside of the tradeoff analysis between the two competing objectives.

II. Microchannel Model

A schematic of a rectangular microchannel heat sink optimized in the current study is shown in Fig. 1. Application of the microrib in the microchannels should not be impractical from manufacturing and design points of view. Therefore, rectangular ribs are chosen as passive heat transfer augmentation structures. The dimensions of the heat sink under consideration are $10 \times 10 \times 0.5$ mm. A silicon-based microchannel can be fabricated for a moderate aspect ratio (H_c/W_c) using KOH wet etching [1,7], whereas for a high aspect ratio and complex geometries, it can be fabricated using other sophisticated techniques such as anisotropic etching, LIGA (lithography, electroplating, molding), and DRIE (deep reactive-ion etching) [23]. In view of the previous optimizations [15–18], a nearly optimum design of a smooth microchannel heat sink with $\theta = 0.175$ and $\phi = 0.075$ with a channel depth H_c of 400 μm is taken for the present study. Staggered microribs are placed at both side walls of the microchannel, which comprise a large part of the channel surface area subjected to wall heat transfer, as shown in Fig. 2. Simulations are performed by varying geometric parameters of the heat sink. A uniform heat flux is applied at the bottom of the heat sink to elucidate the effect of the microchannel geometry on the thermal resistance and pumping power.

III. Numerical Methods

Governing equations for conservation of mass, momentum, and energy for the conjugate heat transfer in the microchannel can be written in vector form as

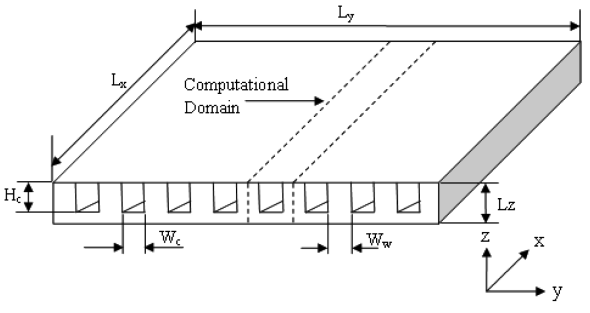

Fig. 1 Schematic diagram of the microchannel heat sink.

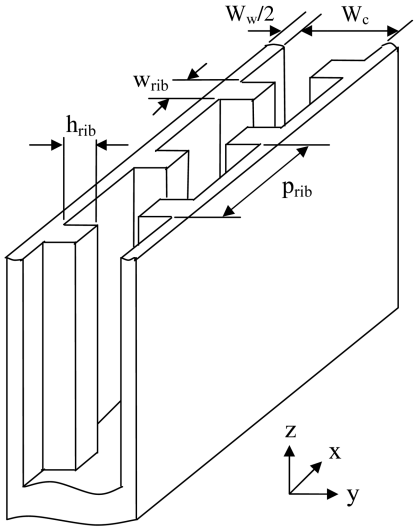

Fig. 2 Schematic of the rib structure.

Mass:

$$\nabla \cdot (\rho_f \bar{V}) = 0 \tag{1}$$

Momentum:

$$\bar{V} \cdot \nabla(\rho_f \bar{V}) = -\nabla p + \nabla \cdot (\mu_f \nabla \bar{V}) \tag{2}$$

Energy for the fluid:

$$\bar{V} \cdot \nabla(\rho_f C_{p,f} T_f) = \nabla \cdot (k_f \nabla T_f) \tag{3}$$

Energy for the substrate conduction:

$$\nabla \cdot (k_s \nabla T_s) = 0 \tag{4}$$

The flow is assumed to be steady, incompressible, and laminar, and radiation effects are neglected. Thermodynamic and hydrodynamic properties of the coolant are assumed to be constant (density $\rho_f = 997$ kg/m^3, specific heat capacity $C_{p,f} = 4.179$ J/kg K, dynamic viscosity $\mu_f = 8.55 \times 10^{-4}$ kg/ms, and thermal conductivity $k_f = 0.613$ W/mK) at a reference temperature of 27°C to save computational expenses and time in the optimization process.

The governing equations were solved using commercial code ANSYS CFX 11.0 [24]. The code uses finite volume discretization of governing differential equations, and the solution was based on the semi-implicit method for pressure-linked equations (SIMPLE) algorithm [25]. Because of symmetry of the microchannels, a single microchannel was selected as the computational domain, as shown in Fig. 1. To implement the practical conditions of the rate of heat transfer at the fluid–solid interface of the ribbed channel, the full length of the microchannel was taken into consideration, comprising ribs on both of the side walls of the microchannel. A hexahedral mesh was generated in the specified computational domain.

Water flows into the microchannel at the inlet of the heat sink and leaves at the outlet; the remainder of the heat sink is occupied by the silicon substrate. The silicon part of the heat sink at the inlet and outlet of the channel is maintained as an adiabatic boundary. A no-slip condition is applied at the interior walls of the channel (i.e., $\bar{V} = 0$). For the conservative analysis of the heat transfer enhancement and optimization, the thermal conditions in the z direction are [15]

$$-k_s \frac{\partial T_s}{\partial z} = q \quad \text{at} \quad z = 0 \quad \text{and} \quad k_s \frac{\partial T_s}{\partial z} = 0 \quad \text{at} \quad z = L_z$$

The left and right surfaces of the computational domain shown in Fig. 1 are assigned as symmetric boundary conditions.

The local Nusselt number can be calculated as

$$Nu = \frac{h_{\text{conv}} d_h}{k_f} = \frac{q_{sf} d_h}{(T_b - T_s) k_f}$$

The bulk temperature can be defined as

$$T_b = \frac{\int_{A_c} uT \, \mathrm{d}A_c}{\int_{A_c} u \, \mathrm{d}A_c}$$

IV. Optimization Techniques

A. Design Variables and Objective Functions

Three design variables, h_{rib}/W_c (α), $w_{\text{rib}}/h_{\text{rib}}$ (β), and W_c/p_{rib} (γ), are chosen for the optimization and design points are selected using three-level fractional factorial design. Table 1 shows these design variables with their ranges. In this work, two different objective functions are employed to optimize the microchannel heat sink: one is thermal resistance related to the heat transfer performance, and the other is pumping power to drive the coolant through the microchannel. Thermal resistance is defined by

$$R_{\text{th}} = \frac{\Delta T_{\max}}{q A_s} \tag{5}$$

where A_s is area of the base of the substrate subjected to heat flux, and $\Delta T_{\max}$ is the maximum temperature rise in the heat sink, defined as

$$\Delta T_{\max} = T_{s,o} - T_{f,i} \tag{6}$$

where $T_{s,o}$ is the substrate temperature near the outlet, and $T_{f,i}$ is the fluid inlet temperature.

The pumping power required to drive the fluid through microchannel heat sink can be evaluated as

$$P = n \cdot u_{\text{avg}} \cdot A_c \cdot \Delta p \tag{7}$$

where Δp is the pressure drop, n indicates the number of channels, u_{avg} is the average velocity, and A_c is the cross-sectional area of the microchannel.

The two objectives are competing in nature, because the decrease in pumping power leads to an increase in thermal resistance. These objective functions are calculated by solving Navier–Stokes and heat conduction equations at specified design points for a constant Reynolds number. Polynomial response-surface curves [22] are generated for individual objectives with the help of CFD calculations, and a hybrid multi-objective evolutionary approach is applied to obtain Pareto-optimal solutions.

B. Surrogate Construction

Evolutionary algorithms require many evaluations for objective functions to search the optimum solutions. Therefore, to evaluate these objective function values, a surrogate is constructed to avoid experimental or numerical expenses and to save time. Queipo et al. [26] suggested application of various surrogate models, including second-order polynomial approximation, for speeding up multi-objective optimization of a liquid rocket injector. In the present study, a RSA method is applied to evaluate objective function values. Response-surface approximation is a methodology of fitting a polynomial function for discrete responses obtained from numerical calculations. It signifies the association between response functions and design variables. For a set of N design variables x_j, the linear

Table 1 Design variables and design space

	Design variables		
Ranges of variables	α (h_{rib}/W_c)	β ($w_{\text{rib}}/h_{\text{rib}}$)	γ(W_c/p_{rib})
Lower	0.3	0.5	0.056
Upper	0.5	2.0	0.112

response function is formulated as

$$f_i = \sum_{j=1}^{N} \zeta_j x_{ij} + \varepsilon_i \tag{8}$$

where errors ε_i are independently distributed and with zero mean and variance σ^2; that is,

$$E(\varepsilon_i) = 0 \quad \text{and} \quad V(\varepsilon_i) = \sigma^2 \tag{9}$$

In the matrix form, Eqs. (8) and (9) can be expressed as

$$f = \mathbf{X}\boldsymbol{\zeta} + \varepsilon \tag{10}$$

$$E(\varepsilon) = 0 \quad \text{and} \quad V(\varepsilon) = \sigma^2 \mathbf{I} \tag{11}$$

where f is a column matrix of M responses, and X is an $M \times N$ matrix of design variable values. The least-squares estimate of ζ is

$$\hat{\zeta} = (\mathbf{X}^{\mathrm{T}}\mathbf{X})^{-1}\mathbf{X}^{\mathrm{T}} f \tag{12}$$

The constructed second-order polynomial response can be expressed as

$$f(x) = \zeta_0 + \sum_{j=1}^{N} \zeta_j x_j + \sum_{j=1}^{N} \zeta_{jj} x_j^2 + \sum \sum_{i \neq j}^{N} \zeta_{ij} x_i x_j \tag{13}$$

For the second-order polynomial model used in the current study, the number of regression coefficients is $(N + 1) \times (N + 2)/2$.

C. Multi-Objective Evolutionary Algorithm

The preceding multi-objective optimization problem is formulated as follows:

Minimize

$$\bar{f}(\bar{x})$$

with the M function to be optimized.

Subject to

$$\bar{g}(\bar{x}) \leq 0$$

with s inequality constraints.

Subject to

$$\bar{h}(\bar{x}) = 0$$

with t equality constraints, where

$$\bar{f}(\bar{x}) = \{f_1(\bar{x}), f_2(\bar{x}), f_3(\bar{x}), \ldots, f_M(\bar{x})\}$$

is a vector of M real-valued objective functions, $\bar{x}$ is a vector of N design variables, $\bar{x} \in R^N$, $\bar{g}(\bar{x}) \in R^s$, and $\bar{h}(\bar{x}) \in R^t$. The present problem is associated with two competing objectives in which improvement of one objective leads to deterioration of other objective. Each feasible solution set $\bar{x}$ of the multi-objective problem is either dominated or nondominated, in which all nondominated solutions are called Pareto-optimal solutions. Vector $\bar{x}_i$ dominates a vector $\bar{x}_j$ if $\bar{x}_i$ is at least as good as $\bar{x}_j$ for all objectives and $\bar{x}_i$ is strictly better than $\bar{x}_j$ for at least one objective.

The methodology used to generate the global Pareto-optimal front is shown in Fig. 3. Objective functions are defined mathematically and evaluated on the data obtained by numerical simulation. A hybrid multi-objective evolutionary approach [21] is used to obtain global Pareto-optimal solutions. In this method, first, approximate Pareto-optimal solutions are obtained using real-coded NSGA-II developed by Deb et al. [20] for two objective functions: thermal resistance and pumping power. Here, real-coded means that the crossover and mutations are conducted in real space to obtain a response of NSGA-II. These solutions are then refined by searching a local optimal solution for each objective function over the whole NSGA-II-obtained optimal solution using sequential quadratic programming with NSGA-II solutions as initial guesses. The sequential quadratic programming is a generalization of Newton's method, which is a gradient-based optimization technique. To perform the local search two approaches are usually applied [21]. In one approach, all the objectives are combined into a single composite objective and the optimum is searched. In another approach, one objective is optimized, treating the others as equality constraints, and the process is repeated to all objectives. In the present study, the first objective is optimized and the second objective is treated as an equality constraint. The local search is repeated for the second objective function, treating the first as an equality constraint. This process gives two new sets of optimal solutions; those are then merged with the NSGA-II solutions. From these solutions, the first dominated solutions are discarded and then duplicate solutions are removed to get global Pareto-optimal solutions. The process of the local search improves the quality of Pareto-optimal solutions.

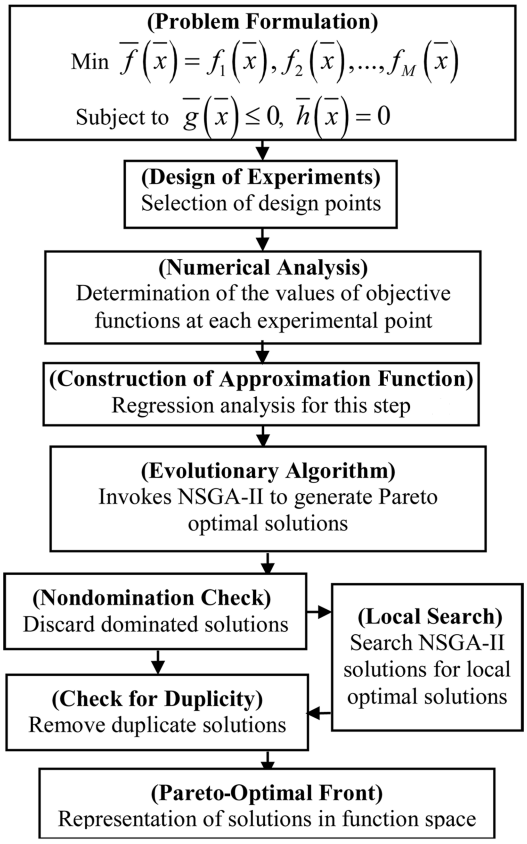

Fig. 3 Multi-objective optimization procedure.

D. *K*-Mean Clustering

After a local search, there were 301 global Pareto-optimal solutions. To find representative solutions from the Pareto-optimal front, these solutions were grouped into seven clusters, applying *K*-mean clustering [27]. It is an iterative alternating fitting process to form the number of specified clusters. These clusters are distributed uniformly along the Pareto-optimal front.

V. Results and Discussion

In this work, a $501 \times 41 \times 61$ grid is used for a geometry of design variables $\alpha = 0.3$, $\beta = 1.25$, and $\gamma = 0.084$. Grid independency is checked by taking different grids in all Cartesian directions; it was found that in comparison with the $501 \times 41 \times 61$ grid, a $556 \times 46 \times 76$ grid shows the change in the highest temperature in the substrate within 0.2%, whereas a $301 \times 31 \times 41$ grid shows more than 1% change. Numerical solutions were validated for a smooth microchannel by Husain and Kim [18], who used the same analysis methods as in this work for a wide range of Reynolds number. In the

preceding validation of the numerical scheme, half of the microchannel was used, accessing the advantage of symmetry. Further validation of the numerical results for a microchannel with rib is performed with the experimental results of Hao et al. [28], as shown in Figs. 4 and 5, in which numerical results show good agreement with the experimental data.

The present model is applicable to both macro- and microflows, though the temperature dependence of properties (variable properties) plays an important role in microflows when heat transfer occurrence is due to scaling effects with respect to different orders of magnitude of Reynolds number and axial temperature gradient [30]. The flow is assumed to be steady, incompressible, and laminar. Heat transfer analysis was performed in terms of Nusselt number. Spanwise-averaged Nusselt numbers are evaluated at different locations in flow direction for a smooth microchannel at constant mass flow rate and compared with the average Nusselt number obtained by Shah and London [31] and Copeland [32], as shown in Fig. 6. The Nusselt number is averaged over the line on three interfaces, except the top wall, which is kept adiabatic. For fully developed flow in a three-side-heated smooth microchannel, the Nusselt number was presented by Shah and London [31] as

$$Nu_{\text{fd}} = 8.235(1 - 1.883\theta + 3.767\theta^2 - 5.814\theta^3 + 5.361\theta^4 - 2\theta^5) \tag{14}$$

Taking into account the thermal entrance-length effect, the equation was fitted on the data from Shah and London [31] by Copeland [32] for the mean Nusselt number as

$$Nu_{\text{mean}} = [\{2.22(x^*)^{-0.33}\}^3 + \{-0.02 + 8.31G\}^3]^{1/3} \tag{15}$$

where the distance along the channel in the thermal entrance region x^* is characterized as $x^* = x/Red_hPr$. Higher values of Nusselt number are found near the inlet, due to the entrance effects. The rate of heat transfer is higher at the top of the rib and lower at the upstream and downstream of the rib, as shown in Fig. 7. The fluid deflected by the rib reaches the opposite wall with higher velocity due to the reduction in flow area, which leads to the higher rate of heat transfer on the opposite wall and rib. The loss of velocities just upstream of the rib and the recirculation due to the sudden expansion of the fluid just downstream of the rib lead to the formation of higher temperature zones at these locations, shown in Fig. 8, due to lower heat transfer than the other locations on the surface. The higher velocity of the mainstream bulk flow separated by shear layer with the recirculating flows at downstream leads to the higher heat transfer on the wall opposite to rib. The shear layer then reattaches to the walls at a point away from the rib and a new boundary layer develops, which reaches to the next rib and develops a very small region of recirculation upstream of the next rib. The two-dimensional projections of streamlines on the planes perpendicular to the main flow are shown in Fig. 9. The turning of streamlines near the rib upstream results in low-intensity recirculation, whereas the turning of streamlines near and on the rib downstream intensifies recirculation, which helps the

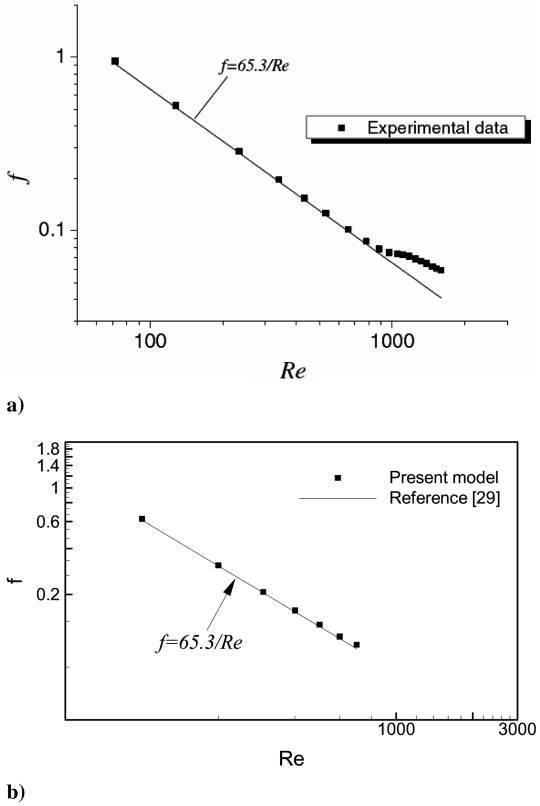

Fig. 4 Comparison of numerical model predictions with experimental results for a rough microchannel ($d_h = 154$ μm): a) experimental results [28] and b) present numerical model.

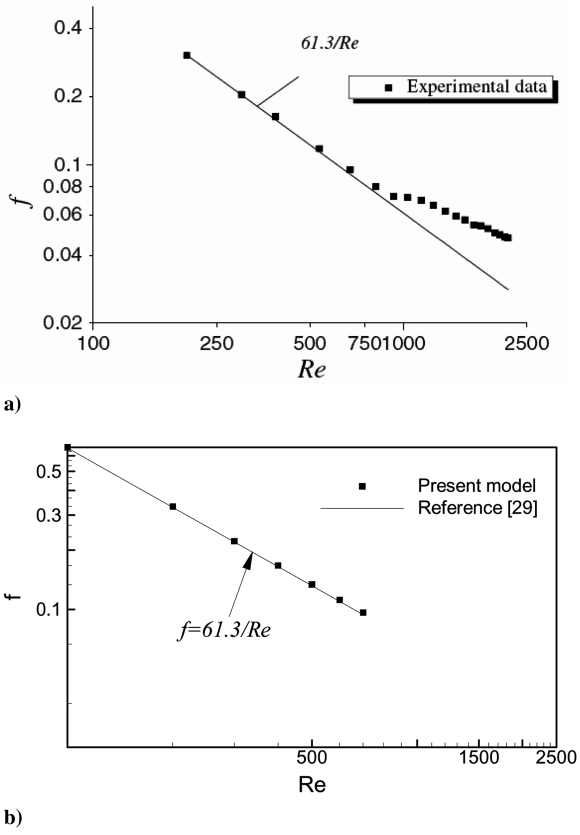

Fig. 5 Comparison of numerical model predictions with experimental results for a rough microchannel ($d_h = 191$ μm): a) experimental results [28] and b) present numerical model.

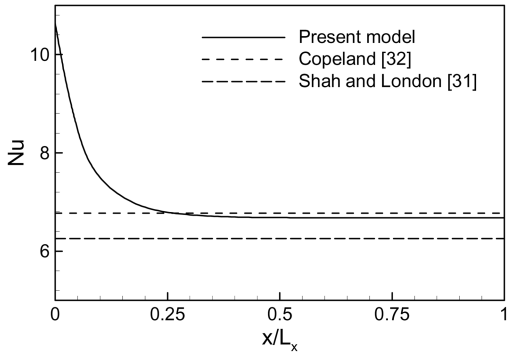

Fig. 6 Spanwise-averaged Nusselt number distributions in flow direction for a smooth microchannel and comparison with mean Nusselt numbers by Shah and London [31] and Copeland [32].

reaches to the next rib and develops a very small region of recirculation upstream of the next rib. The two-dimensional projections of streamlines on the planes perpendicular to the main flow are shown in Fig. 9. The turning of streamlines near the rib upstream results in low-intensity recirculation, whereas the turning of streamlines near and on the rib downstream intensifies recirculation, which helps the

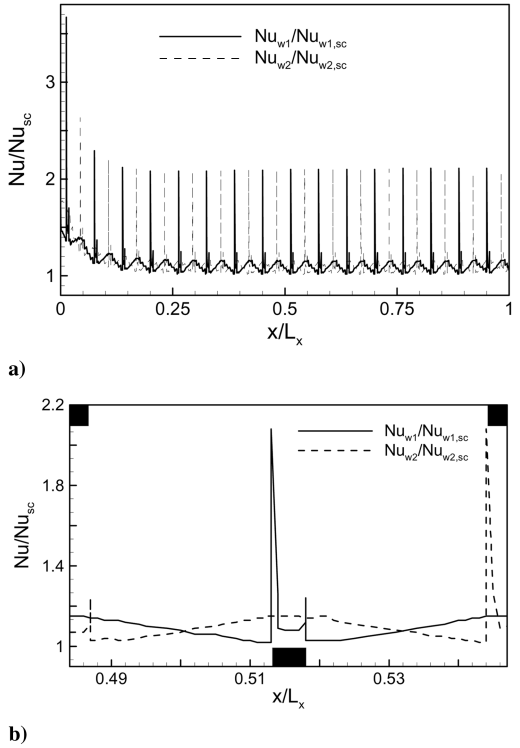

Fig. 7 Normalized Nusselt number distributions on the line along the flow direction at the midheight of the channel for $\alpha = 0.4$, $\beta = 2.0$, and $\gamma = 0.112$ at $z/L_z = 0.6$ for a) full length and b) pitch length.

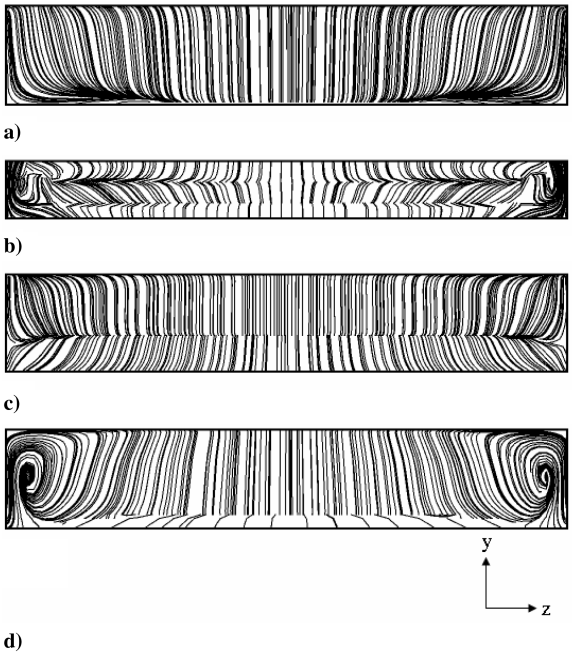

Fig. 9 Streamlines on y–z planes for $\alpha = 0.4$, $\beta = 2.0$, and $\gamma = 0.112$ at a) $x/L_x = 0.5123$, b) $x/L_x = 0.5156$, c) $x/L_x = 0.5189$, and d) $x/L_x = 0.5325$.

secondary flow development in the flow direction, as shown in Figs. 9a–9c. Boundary layers at the top and bottom walls of the microchannel are influenced by the rib and a secondary flow develops within it. The flow then rolls up laterally, which in turn results in large vortical structures in the crossflow direction away from the rib, as shown in Fig. 9d. Distributions of the normalized streamwise vorticity on the planes perpendicular to the main flow direction are shown in Fig. 10. The streamwise vorticity $(\partial w/\partial y - \partial v/\partial z)$ is normalized by the ratio of average velocity to hydraulic diameter (u_{avg}/d_h). The front surface of the rib is located at $x/L_x = 0.5128$. The presence of intense secondary flow just upstream of the rib results in high vorticity in this region, especially at the corners, as shown in Fig. 10a. The intensity of vorticity becomes lower over the rib surface, but further increases as the fluid moves downstream of the rib, due to the presence of higher magnitude of secondary flows that expand laterally toward the center from the walls in Figs. 10b and 10c. At a plane downstream away from the rib, vorticity becomes relatively weak but covers a larger flow region, as shown in Fig. 10d. The streamwise vorticity increases again as the next rib is approached.

Thermal resistance and pumping power for a ribbed microchannel was critically analyzed and compared with the smooth microchannel to attain insight into the advantages associated with the ribbed microchannel heat sinks. Figures 11a and 11b show the variation of thermal resistance and pumping power with mass flow rate. In Fig. 11a, the thermal resistances in the ribbed channels are smaller than those in a smooth channel at same mass flow rate, and they decrease with an increase of mass flow rate at a higher rate in a ribbed microchannel than in a smooth microchannel. But for the same mass flow rate, the pumping power in a ribbed channel is much higher than in a smooth channel, and the rate of increase of pumping power with the mass flow rate is also higher in a ribbed microchannel, as shown in Fig. 11b. Thus, the thermal resistance is decreased by a ribbed structure for a fixed mass flow rate at the expense of higher pressure drop or pumping power. Figure 11c shows the correlation of the two conflicting objective functions: thermal resistance and pumping power. The mass flow rate at a given pumping power is first calculated in a way similar to that by Husain and Kim [18], and thermal resistance is then calculated by numerical simulation.

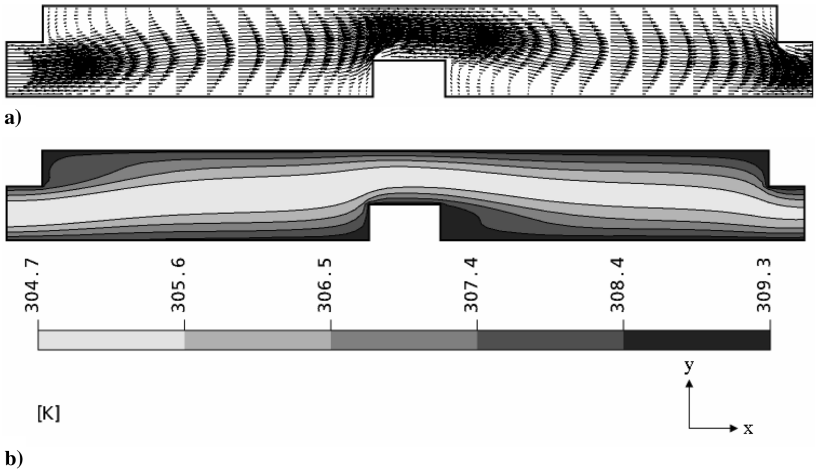

Fig. 8 Velocity and temperature fields on x–y planes at $z/L_z = 0.6$ for $\alpha = 0.4$, $\beta = 2.0$, and $\gamma = 0.112$: a) velocity vectors and b) temperature contours.

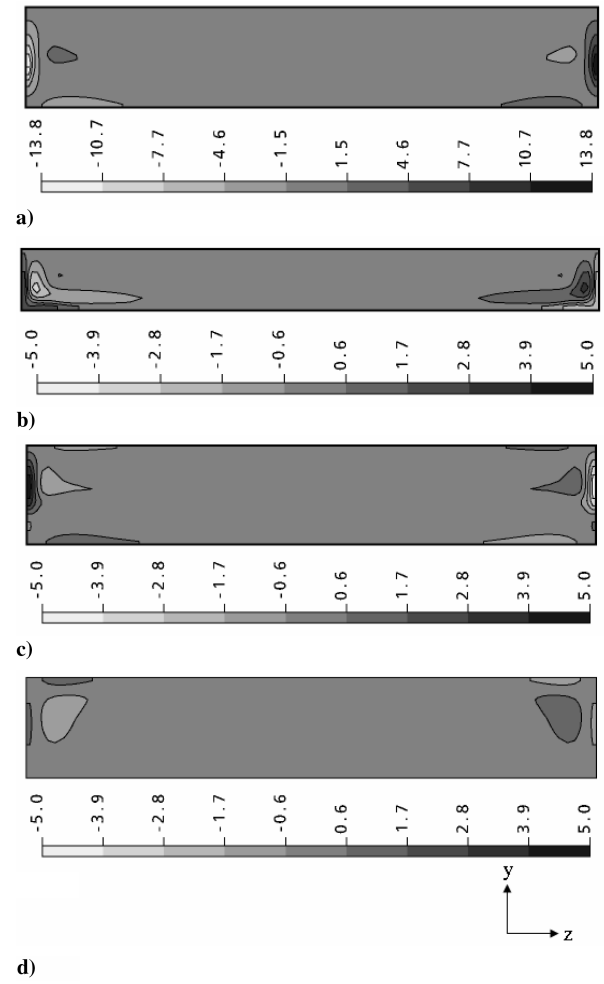

Fig. 10 Normalized streamwise vorticity distributions on y–z planes for $\alpha = 0.4$, $\beta = 2.0$, and $\gamma = 0.112$ at a) $x/L_x = 0.5123$, b) $x/L_x = 0.5156$, c) $x/L_x = 0.5189$, and d) $x/L_x = 0.5325$.

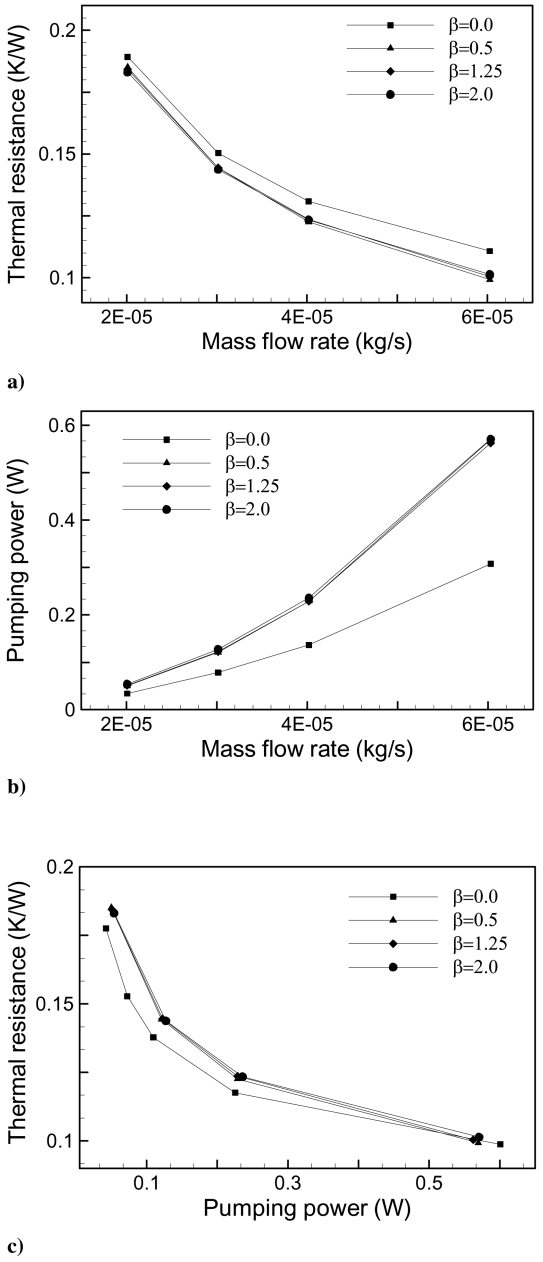

Fig. 11 Variations of thermal resistance and pumping power with mass flow rate and variations of thermal resistance with pumping power in smooth ($\beta = 0.0$) and ribbed microchannels ($\alpha = 0.3$ and $\gamma = 0.112$): a) thermal resistance, b) pumping power, and c) thermal resistance versus pumping power.

Thermal resistance in ribbed channels is generally higher than in smooth channels in the range of pumping power, shown in Fig. 11c, but the rate of decrease of thermal resistance in a ribbed microchannel is higher than with a smooth microchannel, and beyond a certain pumping power, thermal resistance in the ribbed microchannel becomes lower than in the smooth microchannel. As shown in Fig. 11b, the mass flow rate associated with pumping power is much higher in the smooth channel than in the ribbed channel. Thus, the lower thermal resistance in a smooth channel in Fig. 11c is due to the higher mass flow rate in the smooth channel. However, the difference in thermal resistance shown in this figure becomes smaller as pumping power increases, because the advantage of the ribbed structure in enhancing heat transfer increases with mass flow rate, as shown in Fig. 11a. Therefore, it is found from the preceding discussion that the advantage of the ribbed structure strongly depends on the design condition of the ribbed microchannel, and the effect of each design variable on the performance of the microchannel heat sink needs to be investigated.

Design variables contribute differently to the objective functions. Sensitivity analysis was performed to find the respective contribution of design variables to the objective functions. Figure 12 shows the variation of objective functions with the variation of design variables around the center point in the design space: $\alpha = 0.4$, $\beta = 1.25$, and $\gamma = 0.084$. Each design variable is varied around this point in both directions, while keeping the other variables fixed. The objective function values at these sets of design variables are calculated using the surrogate model. Objective functions, thermal resistance, and pumping power are most sensitive to the design variable α, whereas these objective functions are least sensitive to β. The height of the rib is primarily responsible for the generation of secondary flow, which is further intensified by the top and bottom wall interactions. Because the placement of the next rib in the flow direction is away from the reattachment of the shear layer, even in the extreme cases, the pitch of the rib is the less effective factor to the objective functions. It can be seen that any change in design variables leads to small changes in thermal resistance and significant change in pumping power.

Initially, 24 design points are chosen in the design space by fractional factorial design, and objective functions are calculated numerically at these points. With these computational data, the RSA method is used to evaluate objective functions values required at many locations in the search of optimum solutions. In the RSA method, analysis of variance and a regression analysis provided by t statistics [22] are implemented to measure the uncertainty in the set of coefficients in the polynomial. The values of R^2 and R^2_{adj} and the prediction error sum of squares for second-order curve-fitting are given in Table 2. These values are reliable in reference to the value of

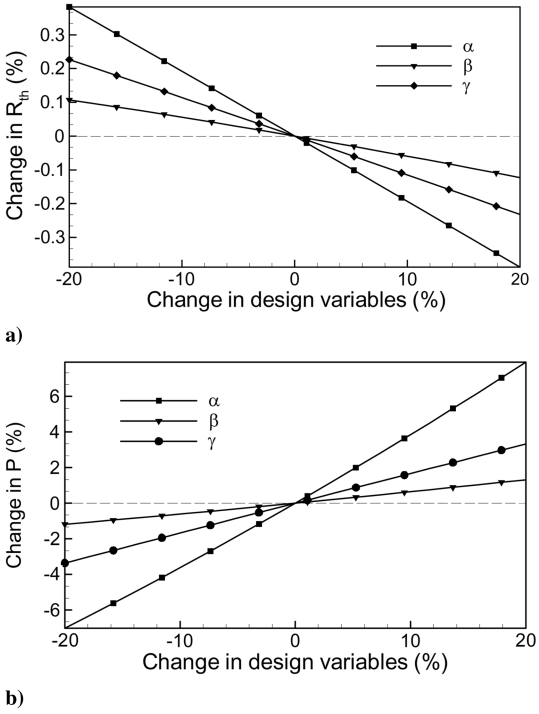

Fig. 12 Sensitivity analysis for ribbed channel with $\alpha = 0.4$, $\beta = 1.25$, and $\gamma = 0.084$: a) thermal resistance and b) pumping power.

$0.9 < R^2_{\text{adj}} < 1.0$ suggested by Giunta [33] for accurate prediction of the response-surface model. The functional forms of the objective functions obtained by RSA in this work are represented as

$$R_{\text{th}} = 0.186 - 0.004\alpha + 0.001\beta - 0.001\gamma - 0.002\alpha\beta - 0.004\alpha\gamma - 0.002\beta\gamma - 0.001\alpha^2 - 0.001\beta^2 - 0.001\gamma^2 \quad (16)$$

$$P = 0.043 - 0.003\beta + 0.008\gamma + 0.011\alpha\beta + 0.026\alpha\gamma + 0.003\beta\gamma + 0.028\alpha^2 + 0.004\beta^2 - 0.001\gamma^2 \quad (17)$$

The preceding polynomial functions are used to evaluate the objective function values at different locations required by MOEA to search Pareto-optimal solutions. A real-coded NSGA-II is invoked to obtain well-spread approximate Pareto-optimal solutions with 250 generations of 100 populations. The crossover and mutation probabilities are set to 0.95 and 0.25, respectively. The crossover and mutation parameters are decided as 10 and 50, respectively. These parameters are adjusted one by one to suit the nature of the problem. After a local search, there are 301 optimal solutions; those are called *global Pareto-optimal solutions*. K-mean clustering is performed to find a representative solution for a group of solutions. Five representative clusters are formed, as shown in Fig. 13, along with the NSGA-II and global Pareto-optimal solutions. The values of objective functions and corresponding design variables at these five clusters are presented in Table 3.

The shape of the Pareto-optimal front suggests that the two objective functions are convex in nature, and for every fixed value of one objective, there is one optimum value of the other objective function. Each extreme end of the Pareto-optimal front represents a set of the highest value of one objective function and the lowest value

Table 2 Results of analysis of variance and regression analysis

Objective function	Order of polynomial	R^2	R^2_{adj}	Prediction error sum of squares
R_{th}	2	0.995	0.991	2.37e-3
P	2	0.994	0.991	3.8e-4

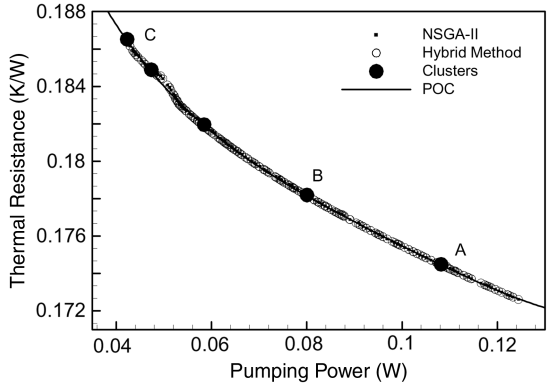

Fig. 13 Pareto-optimal solutions using the hybrid multi-objective evolutionary approach, NSGA-II, five clusters, and global POC.

of the other objective function. Because of the conflicting nature of the objective functions, which was presumed before obtaining the Pareto-optimal front, improvement of one objective leads to deterioration of the other objective. Here, it can be noticed that no solution out of 301 optimal solutions is superior to another in both objectives, because each solution is a global Pareto-optimal solution. The tradeoff analysis shows that at point A, lower thermal resistance is obtained at the expense of higher pumping power, whereas at point C, thermal resistance is higher at lower pumping power. The Pareto-optimal front changes its gradient significantly near point B. A designer can pick the optimal solution according to the pumping power available to drive the fluid or thermal resistance required. A Pareto-optimal curve (POC) is obtained by fitting a fourth-order polynomial for two objectives representing thermal resistance as a function of pumping power, as shown in Fig. 13. The fitness parameters are set as $R^2 = 0.9997$ and $R^2_{\text{adj}} = 0.9997$, and the global mean square error is 6.77×10^{-5}. Only the extent of POC bounded by global Pareto-optimal solutions represents the global Pareto-optimal front. The trend of POC shows that thermal resistance and its gradient decreases with increasing pumping power. It can be seen from the Pareto-optimal front that an efficient tradeoff lies between points 1 and 5 in Table 3.

A deeper insight into the sensitivity can be attained by analyzing the variation of design variables along the Pareto-optimal front, as shown in Fig. 14. This analysis gives designers freedom to choose an economic combination from the design and manufacturing points of view. The distribution of design variables over the Pareto-optimal front is studied by plotting these design variables against both thermal resistance and pumping power, corresponding to the five clusters of Pareto-optimal solutions shown in Fig. 13. It is observed that α shows alternating decreasing and increasing characteristic, whereas β and γ show continuously decreasing characteristics along the optimal front, which is the direction of increasing thermal resistance and decreasing pumping power. The design variable γ is found to be the most Pareto-sensitive (sensitive along the Pareto-optimal front) and its value varies in the entire design range along the Pareto-optimal front, whereas β is found to be the least Pareto-sensitive and α lies between the two. Although the design variable α is found to be the most effective design variable to objective functions (see Fig. 12), the change in its value along the Pareto-

Table 3 Objective functions and design variables for five clusters from global Pareto-optimal solutions

	Design variables				
Clusters	α	β	γ	R_{th}	P
1	0.010	0.528	0.000	0.1865	0.0423
2	0.196	0.996	0.032	0.1849	0.0474
3	0.120	0.995	0.972	0.1820	0.0585
4	0.484	1.000	1.000	0.1782	0.0800
5	0.831	1.000	1.000	0.1745	0.1082

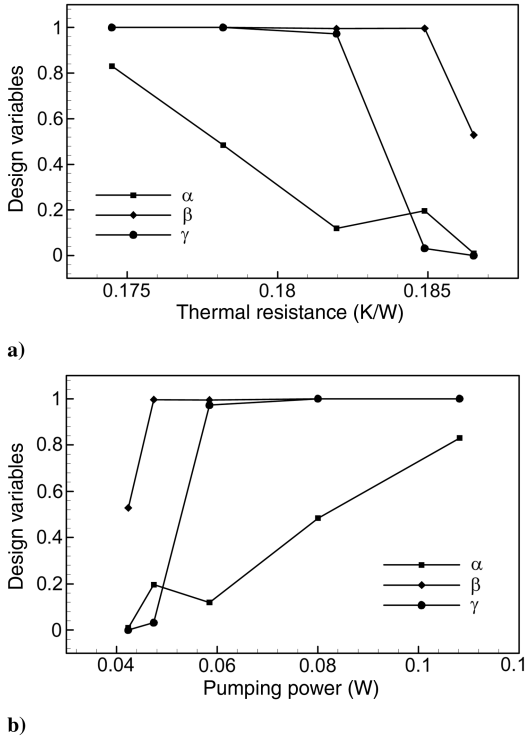

Fig. 14 Distributions of design variables over the Pareto-optimal front with objective functions at clustered locations: a) thermal resistance and b) pumping power.

optimal front is less than the β, which is the least effective design variable.

VI. Conclusions

The present study demonstrates the analysis of a staggered-rib microchannel heat sink and its multi-objective optimization with the help of the hybrid multi-objective evolutionary approach. Design variables related to microrib height, width, pitch, and channel width are selected for optimization purposes. Objective functions, thermal resistance, and pumping power are obtained numerically at specified design points to conduct regression analysis. Global Pareto-optimal solutions are obtained using NSGA-II in combination with a local search strategy. In the view of optimization performed in this study, the following conclusions can be drawn. A Pareto-optimal front reveals the existing tradeoff between thermal resistance and pumping power to optimize the microchannel heat sink. For fixed mass flow rate, rib microstructures decrease thermal resistance at the expense of pumping power higher than the smooth microchannel. Thermal resistance in ribbed channels is generally higher than in smooth channels for fixed pumping power, but the difference in thermal resistance reduces as pumping power increases. Therefore, the advantage of the ribbed structure in the microchannel heat sink strongly depends on the design condition of the microchannel. Although the ratio of rib height to width of channel is found to be the most effective design variable to objective functions, the change in its value over the Pareto-optimal front is less than the ratio of width to height of the rib, which is the least effective design variable. The ratio of channel width to the pitch of the rib shows the highest Pareto sensitivity (sensitivity along the Pareto-optimal front) and its value covers the entire design range, whereas the ratio of width to height of the rib is found to be the least Pareto-sensitive and the ratio of rib height to width of channel lies between the two.

Acknowledgment

This research was supported by the Korea Science and Engineering Foundation (KOSEF) grant funded by the Korean Ministry of Science and Technology (MOST) (no. R01-2006-000-10039-0).

References

[1] Tuckerman, D. B., and Pease, R. F. W., "High-Performance Heat Sinking for VLSI," *IEEE Electron Device Letters*, Vol. 2, No. 5, 1981, pp. 126–129. doi:10.1109/EDL.1981.25367

[2] Samalam, V. K., "Convective Heat Transfer in the Microchannels," *Journal of Electronic Materials*, Vol. 18, No. 5, 1989, pp. 611–617. doi:10.1007/BF02657475

[3] Weisberg, A., Bau, H. H., and Zemel, J. N., "Analysis of the Microchannels for Integrated Cooling," *International Journal of Heat and Mass Transfer*, Vol. 35, No. 10, 1992, pp. 2465–2474. doi:10.1016/0017-9310(92)90089-B

[4] Knight, R. W., Hall, D. J., Goodling, J. S., and Jaeger, R. C., "Heat Sink Optimization with Application to Microchannels," *IEEE Transactions on Components, Hybrids, and Manufacturing Technology*, Vol. 15, No. 5, 1992, pp. 832–842. doi:10.1109/33.180049

[5] Fisher, T. S., and Torrance, K. E., "Optimal Shapes of Fully Embedded Channels for Conjugate Cooling," *IEEE Transactions on Advanced Packaging*, Vol. 24, No. 4, 2001, pp. 555–562. doi:10.1109/6040.982844

[6] Wei, X., and Joshi, Y., "Optimization Study of Stacked Microchannel Heat Sinks for Microelectronic Cooling," *IEEE Transactions on Components and Packaging Technologies*, Vol. 26, No. 1, 2003, pp. 55–61. doi:10.1109/TCAPT.2003.811473

[7] Kawano, K., Minakami, K., Iwasaki, H., and Ishizuka, M., "Development of Micro Channels Heat Exchanging," *Application of Heat Transfer in Equipment Systems, and Education*, edited by, R. A. Nelson, Jr., L. W. Swanson, M.V.A. Bianchi, and C. Camci, American Society of Mechanical Engineers, New York, 1998, pp. 173–180.

[8] Qu., W., and Mudawar, I., "Analysis of Three-Dimensional Heat Transfer in the Microchannel Heat Sinks," *International Journal of Heat and Mass Transfer*, Vol. 45, No. 19, 2002, pp. 3973–3985. doi:10.1016/S0017-9310(02)00101-1

[9] Wei, X. J., Joshi, Y. K., and Ligrani, P. M., "Numerical Simulation of Laminar Flow and Heat Transfer Inside a Microchannel With One Dimpled Surface," *Journal of Electronic Packaging*, Vol. 129, No. 1, 2007, pp. 63–70. doi:10.1115/1.2429711

[10] Cheng, Y. J., "Numerical Simulation of Stacked Microchannel Heat Sink with Mixing-Enhanced Passive Structure," *International Communications in Heat and Mass Transfer*, Vol. 34, No. 3, 2007, pp. 295–303. doi:10.1016/j.icheatmasstransfer.2006.12.007

[11] Wang, X.-Q., Yap, C., and Mujumdar, A. S., "Effects of Two-Dimensional Roughness in Flow in the Microchannels," *Journal of Electronic Packaging*, Vol. 127, No. 3, 2005, pp. 357–361. doi:10.1115/1.1997164

[12] Liou, T.-M., Chen, C.-C., and Tsai, T.-W., "Heat Transfer and Fluid Flow in a Square Duct with 12 Different Shaped Vortex Generators," *Journal of Heat Transfer*, Vol. 122, No. 2, 2000, pp. 327–335. doi:10.1115/1.521487

[13] Ligrani, P. M., Oliveira, M. M., and Blaskovich, T., "Comparison of Heat Transfer Augmentation Techniques," *AIAA Journal*, Vol. 41, No. 3, 2003, pp. 337–362.

[14] Vanderplaats, G. N., *Numerical Optimization Techniques for Engineering Design with Applications*, McGraw–Hill, New York, 1984.

[15] Liu, D., and Garimella, S. V., "Analysis and Optimization of the Thermal Performance of the Microchannel Heat Sinks," *International Journal of Numerical Methods for Heat and Fluid Flow*, Vol. 15, No. 1, 2005, pp. 7–26. doi:10.1108/09615530510571921

[16] Kim, S. J., "Methods for Thermal Optimization of the Microchannel Heat Sinks," *Heat Transfer Engineering*, Vol. 25, No. 1, 2004, pp. 37–49. doi:10.1080/01457630490248359

[17] Li, J., and Peterson, G. P., "'Bud,' Geometric Optimization of a Micro Heat Sink with Liquid Flow," *IEEE Transactions on Components and Packaging Technologies*, Vol. 29, No. 1, 2006, pp. 145–154. doi:10.1109/TCAPT.2005.853170

[18] Husain, A., and Kim, K.-Y., "Shape Optimization of the Microchannel Heat Sink for Micro-Electronic Cooling," *IEEE Transactions on*

Components and Packaging Technologies (to be published).

[19] Foli, K., Okabe, T., Olhofer, M., Jin, Y., and Sendhoff, B., "Optimization of Micro Heat Exchanger: CFD, Analytical Approach and Multi-Objective Evolutionary Algorithms," *International Journal of Heat and Mass Transfer*, Vol. 49, Nos. 5–6, 2006, pp. 1090–1099. doi:10.1016/j.ijheatmasstransfer.2005.08.032

[20] Deb, K., Agrawal, S., Pratap, A., and Meyarivan, T., "A Fast and Elitist Multi-Objective Genetic Algorithm for Multi-Objective Optimization: NSGA-II," *Parallel Problem Solving from Nature (PPSN 6)*, Springer, New York, 2000, pp. 849–858.

[21] Deb, K., and Goel, T., "A Hybrid Multi-Objective Evolutionary Approach to Engineering Shape Design," *Evolutionary Multi-Criterion Optimization*, Springer, London, 2001, pp. 385–399.

[22] Myers, R. H., and Montgomery, D. C., *Response Surface Methodology: Process and Product Optimization Using Designed Experiments*, Wiley, New York, 1995.

[23] Jackson, M. J., *Microfabrication and Nanofabrication*, CRC Press, Boca Raton, FL, 2006.

[24] ANSYS CFX, Software Package, Ver. 11.0, ANSYS, Inc., Canonsburg, PA, 2006.

[25] Patankar, S. V., Numerical Heat Transfer and Fluid Flow, McGraw–Hill, New York, 1980.

[26] Queipo, N. V., Haftka, R. T., Shyy, W., Goel, T., Vaidyanathan, R., and Tucker, P. K., "Surrogate-Based Analysis and Optimization," *Progress in Aerospace Sciences*, Vol. 41, No. 1, 2005, pp. 1–28. doi:10.1016/j.paerosci.2005.02.001

[27] JMP Statistical Discovery, Software Package, Ver. 6.0.0, SAS Inst., Inc., Cary, NC, 2005.

[28] Hao, P.-F., Yao, Z.-H., He, F., and Zhu, K.-Q., "Experimental Investigation of Water Flow in a Smooth and Rough Silicon Microchannels," *Journal of Micromechanics and Microengineering*, Vol. 16, No. 7, 2006, pp. 1397–1402. doi:10.1088/0960-1317/16/7/037

[29] Shah, R. K., and London, A. L., *Laminar Flow Forced Convection in Ducts*, Academic Press, New York, 1978.

[30] Herwig, H., and Mahulikar, S. P., "Variable Property Effects in Single-Phase Incompressible Flows Through Microchannels," *International Journal of Thermal Sciences*, Vol. 45, No. 10, 2006, pp. 977–981. doi:10.1016/j.ijthermalsci.2006.01.002

[31] Shah, R. K., and London, A. L., *Laminar Flow Forced Convection in Ducts: A Source Book for Compact Heat Exchanger Analytical Data*, Academic Press, New York, 1978.

[32] Copeland, D., "Optimization of Parallel Plate Heatsinks for Forced Convection," *Proceedings of the 16th IEEE Semiconductor Thermal Measurement and Management Symposium*, Inst. of Electrical and Electronics Engineers, Piscataway, NJ, 2000, pp. 266–272.

[33] Giunta, A. A., "Aircraft Multidisciplinary Design Optimization Using Design of Experimental Theory and Response Surface Modeling Methods," Ph.D. Dissertation, Virginia Polytechnic Inst. and State Univ., Blacksburg, VA, 1997.